Supplementary Material for "Design of Polar XC_3 (X=P, As, Sb, Bi) Monolayers with Coupled Bandgap, Polarization, and Optical Responses"

Wenxiao Li,[1] Junlan Shi,[1] Jing Chang,[2,*] and Botao Fu[1,*]
[1]College of Physics and Electronic Engineering, Center for Computational Sciences, Sichuan Normal University, Chengdu, 610068, China

(Dated: June 29, 2025)

[2]College of Physics and Electronic Engineering, Sichuan Normal University, Chengdu, 610068, China

(Dated: June 29, 2025)

I THE STRUCTURAL STABILITY OF XC_3

Table S1 collects the optimized lattice parameters of the 2D polar XC_3 (X = P, As, Sb, Bi) monolayers. The lattice constant a increases monotonically with the atomic number of pnictogen, accompanied by a simultaneous rise in the local buckling height h of the X atoms.

To evaluate mechanical stability, we calculated the elastic constants, and the results, summarized in Table S2, indicate that all XC_3 meet the mechanical stability criteria[2], with $C_{11} > 0$, $C_{66} > 0$, and $C_{11} \times C_{22} > C_{12}^2$. These findings collectively validate the mechanical Phonon dispersions computed by density-functional perturbation theory (DFPT)[1] with a 4×4×1 supercell exhibit no imaginary modes anywhere in the Brillouin zone (Fig. S1), evidencing dynamical stability. Ab-initio molecular-dynamics simulations (AIMD)[2] carried out at 300 K for the same supercell show no bond reconstruction or lattice distortion over the 10 ps trajectory (Fig. S2), demonstrating thermal stability.

To assess experimental accessibility we evaluated the binding and formation energies of XC_3 monolayers. The binding energy:

$$E_b = \left(E_X + 3E_C - E_{XC_3}\right)/4$$

is referenced to isolated X and C atoms, while the formation energy

$$E_f = \left(E_C^{bulk} + 3E_X^{bulk} - E_{XC_3}\right)/4$$

uses the most stable bulk allotropes (black P, gray As, rhombohedral Sb, metallic Bi, and graphene) as chemical potentials. The calculated results are presented in Table S2, the binding energies of XC_3 are negative, indicating favorable conditions for synthesis. Among them, AsC_3 has the lowest binding energy only slightly higher than that of graphene. The formation energies of these materials are small positive values (< 0.37 eV/a.u.), with AsC_3 exhibiting the lowest formation energy (0.182 eV/a.u.), suggesting that it might be experimentally synthesized on suitable substrates.

Substitution of P, As, Sb, or Bi for C in graphene forces the sheet into a buckled geometry driven by X-C sp^3 hybridization. The electron-localization function (ELF, Fig. S3) evidences this local tetrahedral coordination, reminiscent of phosphorene or arsenene. Crucially, the electronegativity mismatch polarizes each X-C bond, so every X atom carries a net out-of-plane electric polarization; the resulting charge asymmetry is absent in the isostructural but non-polar group-V sheets.

Table S1 The lattice a ($\AA$), buckling height h ($\AA$), bond length $d_{C\text{-}X}$ ($\AA$), band gap E_g (eV), bandwidth of the band of the Mexican hat ΔE_{HVB} (eV) of XC_3

XC_3	a ($\AA$)	h ($\AA$)	d_{C-X} ($\AA$)	E_g (eV)	ΔE_{HVB} (eV)
PC_3	5.37	0.67	1.82	2.13	1.72
AsC_3	5.57	0.79	1.97	3.05	1.10
SbC_3	5.90	0.89	2.19	3.11	0.34
BiC_3	6.80	0.94	2.30	2.87	0.66

Table S2 The cohesive energy E_c (eV), formation energy E_f (eV), mechanical constant C_{ij} (GPa) of XC_3.

XC_3	E_c (eV)	E_f (eV)	C_{11} (GPa)	C_{22} (GPa)	C_{66} (GPa)	C_{12} (GPa)
PC_3	-7.800	0.371	91.50	91.50	11.03	40.24
AsC_3	-7.801	0.182	71.30	71.30	7.90	31.70
SbC_3	-7.118	0.737	53.88	53.88	7.25	23.31
BiC_3	-6.919	0.862	44.25	44.25	5.13	19.56
Gra.	-9.133	-0.007	175.85	175.85	31.08	72.39

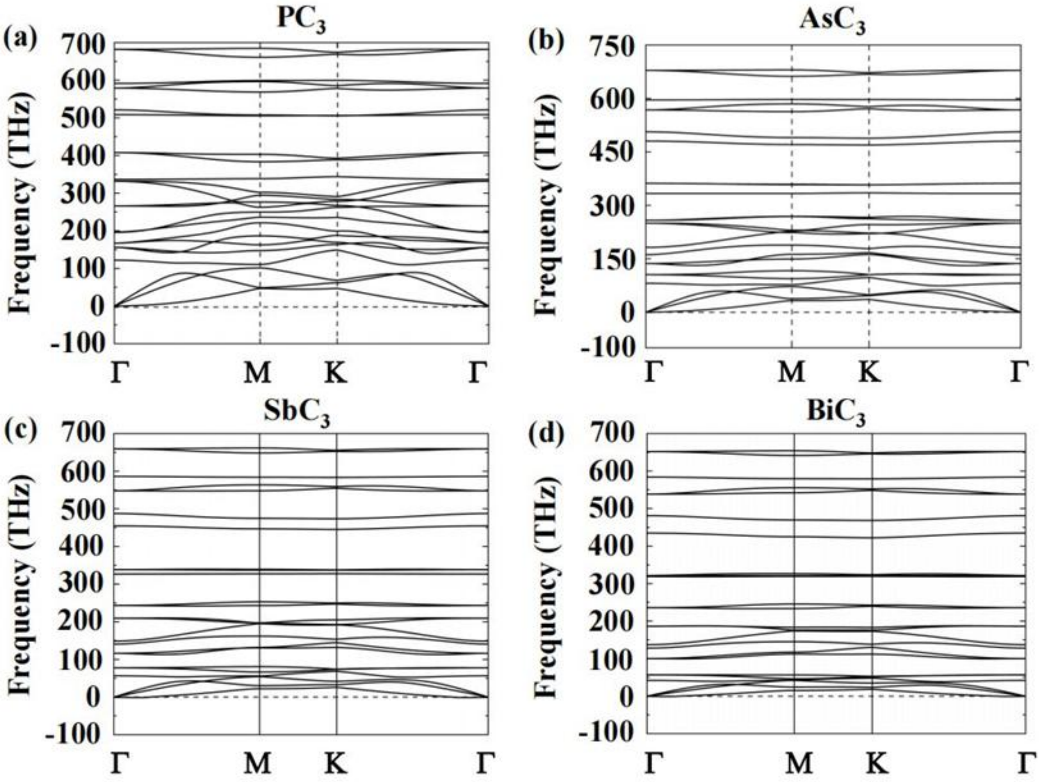

Fig. S1 (a-d) Phonon spectrum of α-XC$_3$.

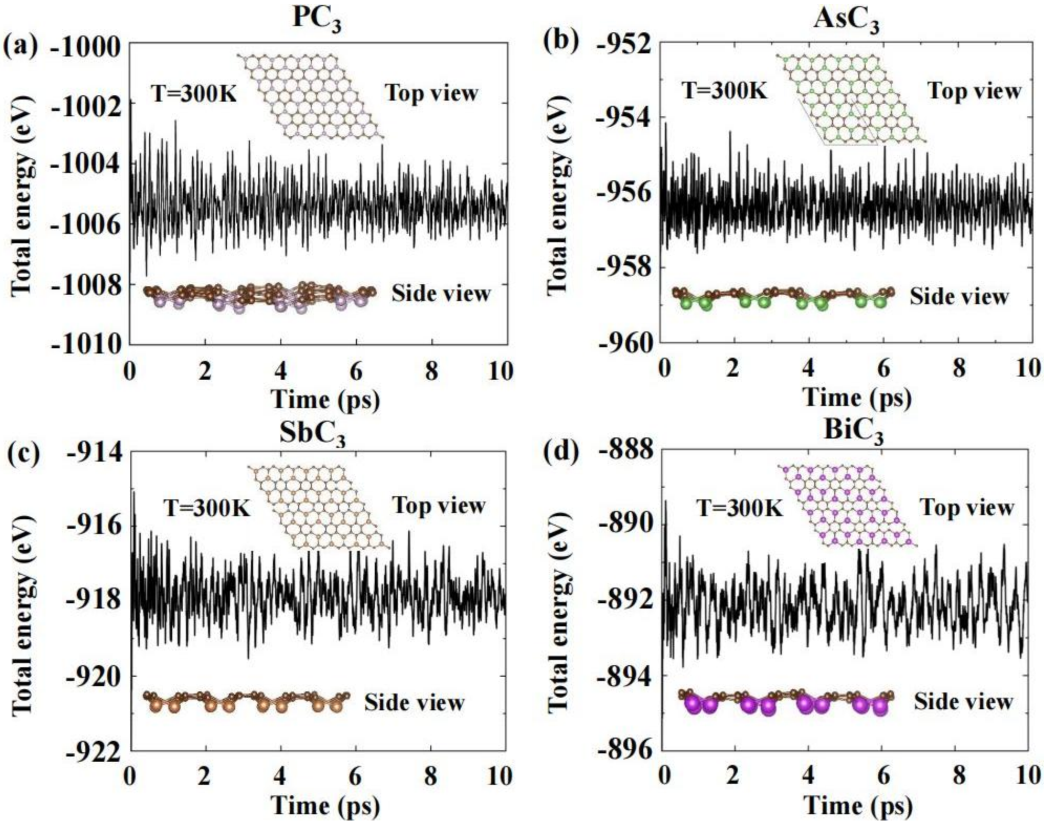

Fig. S2 (a-d) AIMD simulations for α-XC$_3$ under 300 K.

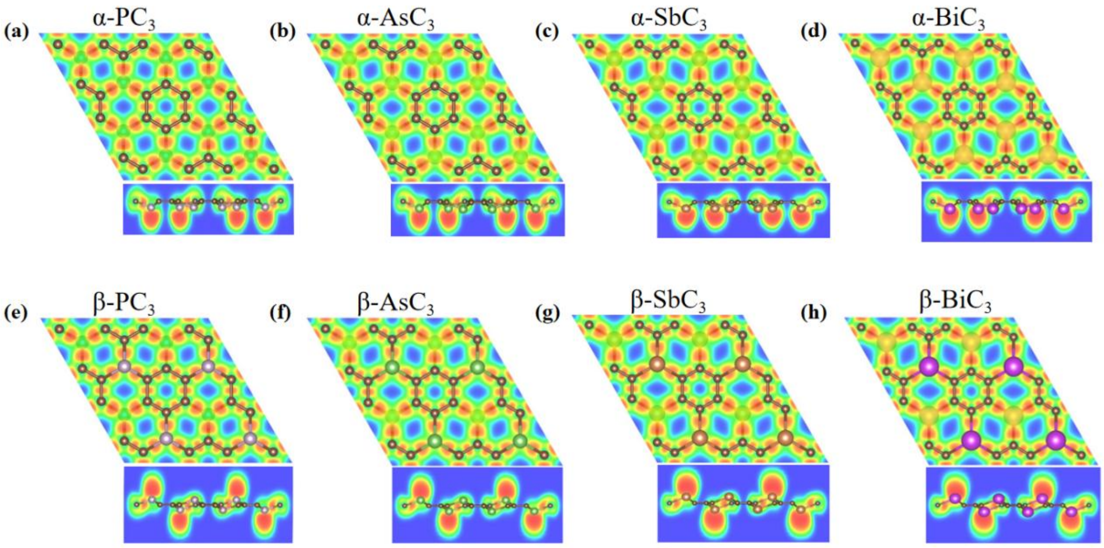

Fig. S3 (a)-(d) are the electron localization function (ELF) of α-XC_3. (e)-(h) are the ELF of β-XC_3.

II OPTICAL PROPERTIES

The optical absorption mechanism of AsC_3 is systematically investigated. As shown in Fig. S4(a), AsC_3 exhibits an absorption peak reaching 4.5×10^5 cm^{-1}, with the first absorption edge located at 4.17 eV. To elucidate the origin of its high absorption coefficient, we calculated the joint density of states (JDOS) and transition dipole moment (TDM) based on Fermi's golden rule.

Fig. S4(c, f) reveals that the local bandgap distribution displays relatively flat dispersion in the red and blue regions, indicating band nesting effects. This arises primarily because the conduction and valence bands exhibit similar dispersion along the Γ-M and Γ-K paths, satisfying momentum-matching conditions, thereby leading to the characteristic band nesting. As highlighted by the pink regions in Fig. S4(b), the nested energy ranges (4.01-4.02 eV and 4.15-4.16 eV) likely contribute to the JDOS peaks. Furthermore, Fig. S4(b) show that the conduction and valence bands at the M point satisfy saddle-point conditions, which may generate pronounced JDOS peaks. Indeed, our JDOS calculations (Fig. S4(e)) confirm a prominent peak near 4.08 eV, attributed to the unique band nesting and saddle-point features of AsC_3.

Fig. S4(d) presents the TDM and local bandgap distribution between the highest valence band (HVB) and lowest conduction band (LCB) along high-symmetry paths. Notably, the TDM near the M-point is significantly enhanced. Along the M-Γ direction, the TDM initially increases and then decreases, while along the M-K direction, it exhibits a more complex trend, Increase first, then decrease, and increase again, reaching maxima near saddle points.

Therefore, we infer that it is the combination of TDM and JDOS contributes to the prominent band-edge absorption, as demonstrated in Fig. S4(a).

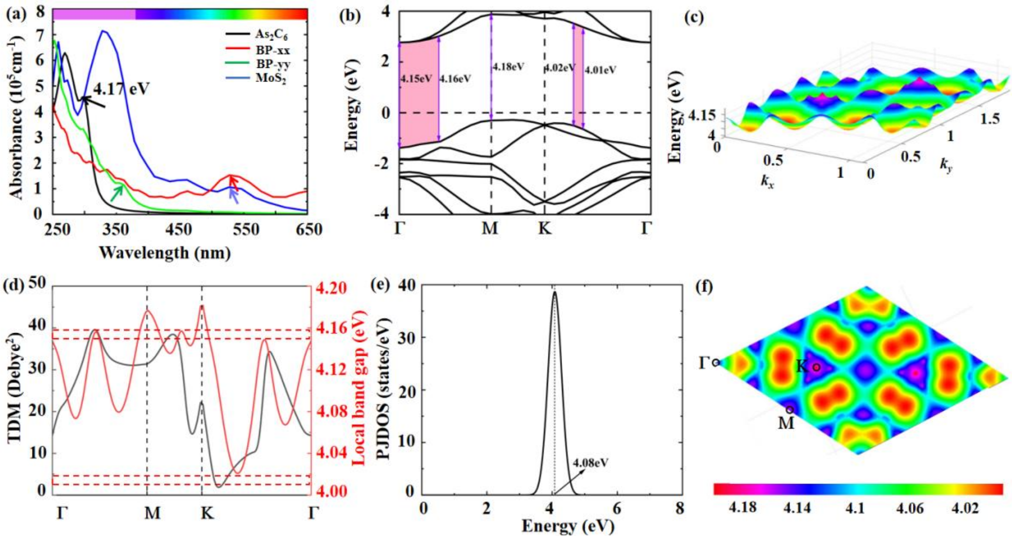

Fig. S4 (a) Optical absorption spectrum of monolayer AsC_3, with those of monolayer MoS_2 and black phosphorene shown for comparison. The arrows indicate the first band-edge absorption peak. (b) Enlarged view of the AsC_3 band structure near the Fermi level, where the shaded pink region highlights the band nesting feature. (c) Side view of the 3D distribution of the local band gap $E_{cv}(\boldsymbol{k})$ in AsC_3. (d) TDM between the HVB and the LCB of AsC_3 (left axis), along with the corresponding local band gap along high-symmetry paths (right axis). (e) Partial JDOS between the HVB and LCB. (f) Top view of 3D distribution of the local band gap $E_{cv}(\boldsymbol{k})$ in AsC_3.

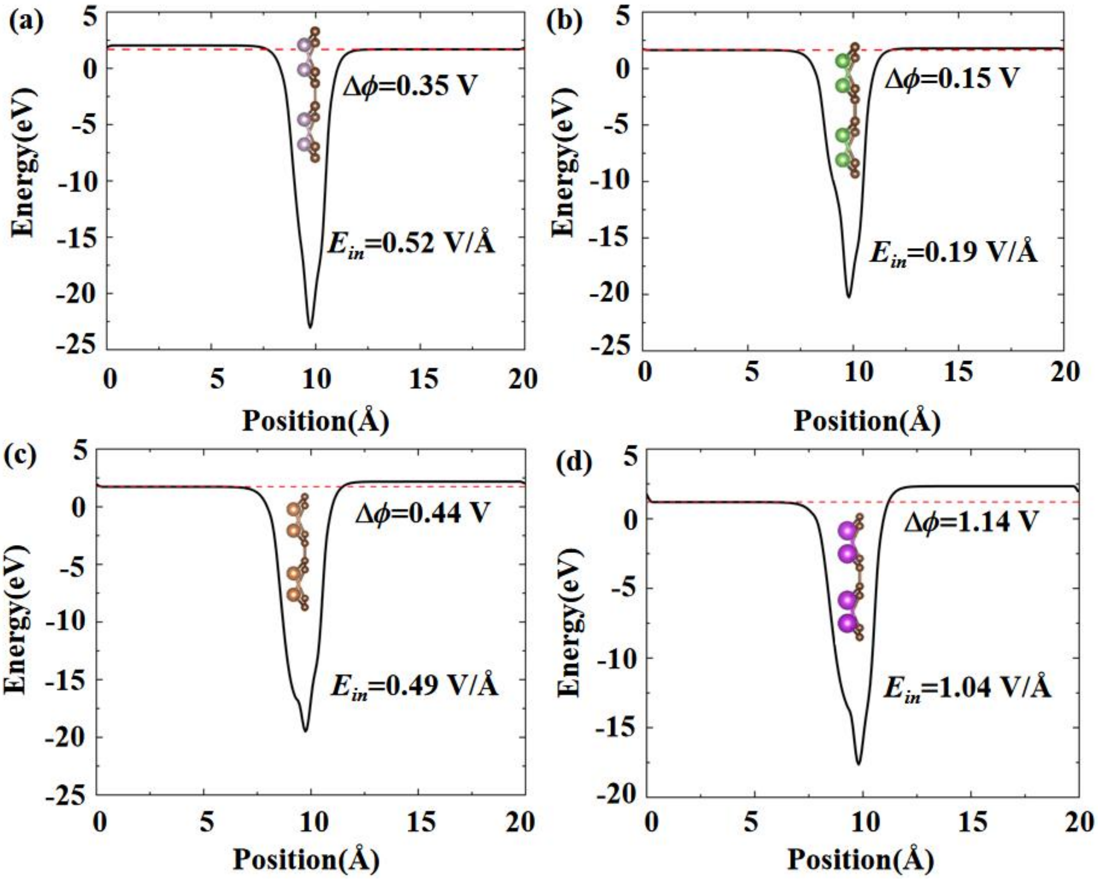

Fig. S5 The electrostatic potential difference $\Delta\phi$ (V) between the two surfaces, and the intrinsic electric field E_{in} (V/Å) of (a) PC_3, (b) AsC_3, (c) SbC_3, (d) BiC_3.

We have further investigated the electronic structures and optical absorption properties of SbC_3 and BiC_3 by explicitly including spin-orbit coupling (SOC) within the HSE06 calculations. As shown in Fig. S6 (a, b), Fig. S6 (a, b) is below. The inclusion of SOC leads to relatively mild modifications in the band structures of both systems. Specifically, the band gaps decrease slightly: for SbC_3, the gap reduces from 3.11 eV to 3.06 eV, and for BiC_3, from 2.87 eV to 2.61 eV. Moreover, near the high-symmetry points (highlighted by red boxes in the Fig. S6 (a, b)), noticeable Rashba-like spin splitting appears in the band dispersions, originating from the absence of spatial inversion symmetry. Notably, the band gap reduction and spin-splitting effects are more pronounced in BiC_3 than in SbC_3, which can be attributed to the stronger SOC inherent to the heavier Bi atom compared to Sb.

As shown in Fig. S6 (c, d), the optical absorption responses of both materials exhibit certain changes upon the inclusion of SOC. Specifically, the band-edge absorption peak of SbC_3 shows a slight redshift from 3.59 eV to 3.57 eV, while its lineshape and intensity remain essentially unchanged. In contrast, BiC_3 displays a more pronounced modification in its optical absorption: its band-edge absorption peak located around 3.61 eV blueshifts to 3.57 eV, accompanied by a significant broadening of the peak shape and a slight reduction in intensity.

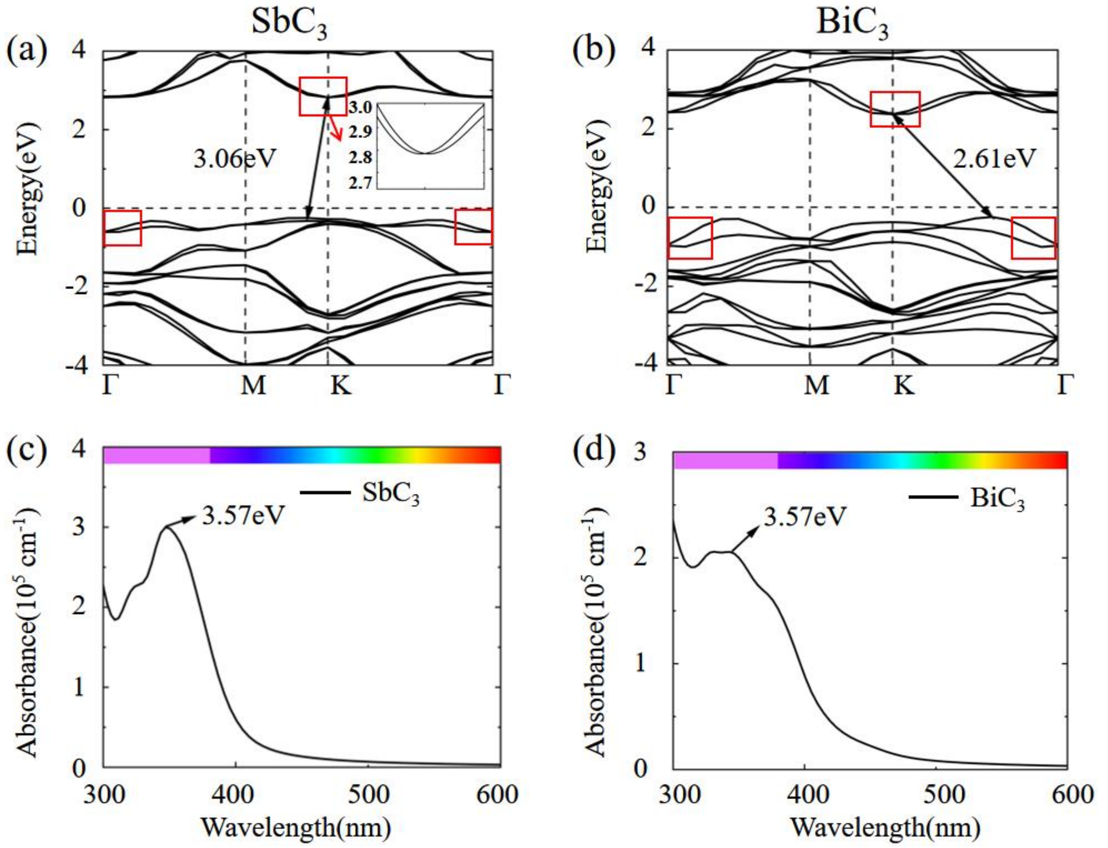

Fig. S6 (a, b) Band structures and (c,d) optical absorption spectra of SbC_3 and BiC_3 monolayers calculated at the HSE06+SOC level.

References

[1] Togo, Atsushi, and Isao Tanaka. "First principles phonon calculations in materials science." *Scripta Materialia* 108 (2015): 1-5.

[2] Barnett, Robert N., and Uzi Landman. "Born-Oppenheimer molecular-dynamics

simulations of finite systems: Structure and dynamics of $(H_2O)_2$." *Physical review B* 48.4 (1993): 2081.

[3] Wang, Vei, et al. "VASPKIT: A user-friendly interface facilitating high-throughput computing and analysis using VASP code." *Computer Physics Communications* 267 (2021): 108033.